J. Fluid Mech. (2013), *vol.* 724, *pp.* 259–283. © Cambridge University Press 2013
doi:10.1017/jfm.2013.138

Shock waves in microchannels

G. Mirshekari[1], M. Brouillette[1,†], J. Giordano[2], C. Hébert[1], J.-D. Parisse[2] and P. Perrier[2]

[1]Department of Mechanical Engineering, Université de Sherbrooke, Sherbrooke, Quebec, Canada J1K 2R1

[2]IUSTI UMR 7343 CNRS – Aix Marseille Université, 5 rue Enrico Fermi, 13453 Marseille, France

(Received 24 September 2012; revised 21 February 2013; accepted 1 March 2013; first published online 29 April 2013)

A fully instrumented microscale shock tube, believed to be the smallest to date, has been fabricated and tested. This facility is used to study the transmission of a shock wave, produced in a large (37 mm) shock tube, into a 34 μm hydraulic diameter and 2 mm long microchannel. Pressure microsensors of a novel design, with gigahertz bandwidth, are used to obtain pressure–time histories of the microchannel shock wave at five axial stations. In all cases the transmitted shock wave is found to be weaker than the incident shock wave, and is observed to decay both in pressure and velocity as it propagates down the microchannel. These results are compared with various analytical and numerical models, and the best agreement is obtained with a Navier–Stokes computational fluid dynamics computation, which assumes a no-slip isothermal wall boundary condition; good agreement is also obtained with a simple shock tube laminar boundary layer model. It is also found that the flow developing within the microchannel is highly dependent on conditions at the microchannel entrance, which control the mass flux entering into the device. Regardless of the micrometre dimensions of the present facility, shock wave propagation in a microchannel of that scale exhibits a behaviour similar to that observed in large-scale facilities operated at low pressures, and the shock attenuation can be explained in terms of accepted laminar boundary models.

Key words: compressible microfluidics, shock waves

1. Introduction

With the miniaturization of engineering technologies down into the millimetre and micrometre ranges, new physical effects may need to be accounted for. For microfluidic devices, these are mostly due to the greater influence of the flow boundaries, which may, among other effects, increase the relative importance of friction and heat transfer. Owing to the large number of applications of incompressible microfluidics, mostly in biology and medicine, the low-Mach-number limit of fluid flow in microchannels has been studied quite extensively (Squires & Quake 2005).

Lately, there has been a similar interest in the characterization of compressible microchannel flows, mostly concerned with the study of steady flow in submillimetre-scale channels, in the continuum and rarefied regimes (Colin 2005). Shock waves represent another type of compressible flow phenomena of great fundamental and practical interest, owing to the unsteady nature of the fluid motion and the potential for

† Email address for correspondence: Martin.Brouillette@USherbrooke.ca

https://doi.org/10.1017/jfm.2013.138 Published online by Cambridge University Press

creating extreme conditions of velocity, pressure, temperature and density. Interestingly, a number of conventional shock wave phenomena incorporate wave propagation and interaction at submillimetre length scales, such as shock wave propagation in porous media (Levy *et al.* 1996), shock wave interaction with turbulence (Mahesh, Lele & Moin 1997), heterogeneous condensed-phase explosives (Lee *et al.* 1995) and shock wave/boundary layer interaction (Dolling 2001). In addition, many new applications utilizing shock waves at small scale are now being developed, for example wave-rotor compressors (Iancu & Muller 2006), micropropulsors (Martel & Brouillette 2003), drug delivery systems (Takayama 1999) and miniaturized explosive devices (Stewart 2002).

The effects of scale on the propagation of shock waves have been examined theoretically by Brouillette (2003), using source terms in a control-volume model to quantify diffusive transport phenomena in narrow channels. This study resulted in modified Hugoniot curves, which account for scale effects as compared to ideal (i.e. large-scale) shock wave phenomena, and the identification of ReD/L as the fundamental scaling parameter, with the Reynolds number $Re \equiv Dc/\nu$, based on the hydraulic diameter of the channel D, the speed of sound c and kinematic viscosity ν of the fluid and the axial extent of the shock region L. Using Rayleigh line analysis, this work also predicted that, for sufficiently small values of the scaling parameter, the propagation velocity of infinitesimal perturbations in perfect gases should be slower than the isentropic speed of sound by a factor $(ReD)/(4\gamma L)$, with γ the ratio of specific heats, in agreement with the result of Kirchhoff (1868) for acoustic wave propagation in viscous channels. For sufficiently small channels, these phenomena may also fall within the rarefied flow regime since the combination of low Reynolds number with high Mach number M may yield sufficiently high Knudsen numbers $Kn \sim M/Re$.

Based on the ReD/L scaling parameter for small-scale shock wave propagation, it is observed that the effects of scale can be increased by either reducing the physical scale of the channel or by increasing the kinematic viscosity of the gas, which can be achieved in practice by decreasing its initial pressure. Indeed, low-pressure shock tube operation has been studied extensively in the past. These flows are dominated by the development of laminar boundary layers behind the shock wave, which leads to a reduction in shock speed for a given diaphragm pressure ratio (Duff 1959), the attenuation of the shock wave (Mirels 1966) and a decrease in test time (Roshko 1960).

Recent experiments on small shock tubes, at normal or reduced pressures, have essentially revealed the same phenomena. For example, Brouillette (2003) has examined the operation of a 5.3 mm shock tube at initial pressures down to 1 mBar for diaphragm pressure ratios up to 10^5 and found, for a given diaphragm pressure ratio, a decrease in shock strength with decreasing scaling parameter ReD/L. Garen *et al.* (2009), using an atmospheric 1 mm shock tube equipped with a quick opening valve instead of diaphragm, corroborated these observations using laser differential interferometry. Austin & Bodony (2011) performed similar experiments with a 5.1 m long 1.65 mm diameter tube initially filled with air or argon at 0.5 or 1 atm and found that shock wave attenuation was mostly due to turbulent boundary layer development behind the shock, in agreement with the model of Mirels (1957).

In parallel, efforts have also been devoted to the numerical simulation of these flows. Using a one-dimensional model with added source terms to account for lateral transport effects, Mirshekari & Brouillette (2009) performed simulations of micrometre-size shock tubes. For a 10 μm shock tube, the result showed the possibility

https://doi.org/10.1017/jfm.2013.138 Published online by Cambridge University Press

of shock wave disappearance at sufficiently low pressure ratios. Similar conclusions were reached by Ngomo *et al.* (2010) with a more sophisticated one-dimensional numerical model. By solving the unsteady two-dimensional Navier–Stokes equations with a slip velocity and a temperature jump at the wall boundary, Zeitoun & Burtschel (2006) also simulated various microscale shock tube flows at low pressure. The results showed strong shock wave attenuation accompanied by a decrease of the hot flow properties along the tube; this lead to the eventual disappearance of the shock for sufficiently low values of the ReD/L scaling parameter. Parisse *et al.* (2009) numerically examined the two-dimensional transmission of a shock wave from a large (100 mm) to a 50 mm long and 100–400 μm wide microchannel and observed increased shock wave attenuation with decreasing microchannel width.

Nevertheless, shock wave phenomena have never directly been observed in submillimetre-scale channels, a first step towards the creation of miniature devices exploiting these flows. This paper presents the results of experiments aimed, for the first time, at the study of shock wave propagation into specially built instrumented micrometre-size channels. Shock waves of Mach numbers ranging from 1.65 to 2.61 are produced in a conventional size shock tube and propagate into a channel having a hydraulic diameter of 34 μm instrumented with novel miniaturized pressure transducers. The experimental details are first described and the data from the experiments are presented. These results are then compared with inviscid and viscous computations and explained in terms of simple analytical models for compressible flow with friction.

2. Experiments

2.1. *Design considerations*

A facility has been specially designed, built and tested for the observation of shock wave propagation in microchannels. A conventional shock tube generally comprises a high-pressure driver section and a low-pressure driven or test section; the two sections are initially separated by either a rupturable diaphragm or a quick opening valve, and appropriate flow instrumentation is located at various axial locations along the tube. Since we are interested in a micrometre-scale facility, scaling down shock tube components poses great technical challenges. Although micrometre-scale channels can be manufactured using available clean-room bulk and surface fabrication techniques, new thinking is required for diaphragm/quick-opening valve operation and instrumentation design.

The burst pressure p_b of a shock tube diaphragm can be shown to scale as $p_b \sim \sigma_t t/D$, where σ_t is the tensile strength of the diaphragm material, t its thickness and D its diameter (Brouillette 1991). To obtain similar burst pressures as in conventional shock tubes using similar materials, the diaphragm thickness then scales with the microchannel diameter. For a channel size of $\sim$10 μm, this means that the required diaphragm thickness should be at least four orders of magnitude thinner than a diaphragm in a conventional shock tube, i.e. in the 10–100 nm thickness range. Leakage of high-pressure driver gas across such a thin membrane could be a problem, assuming that it could be fabricated. Indeed, considering that a micrometre-scale channel would be fabricated by etching into a lateral direction, assembling a nanometre-scale diaphragm at one extremity of the channel in the axial, i.e. perpendicular, direction is quite challenging with existing technologies. Furthermore, flow perturbations introduced by diaphragm obstruction and fragments,

https://doi.org/10.1017/jfm.2013.138 Published online by Cambridge University Press

as well as finite diaphragm opening time, may greatly influence shock formation and propagation at these scales.

Another method for initiating the flow in a shock tube is to use a quick-opening valve between the high- and low-pressure sections (Udagawa *et al.* 2008). This valve should tightly seal both sections to avoid gas contamination and loss of pressure and it should also open sufficiently rapidly to allow shock wave formation within a few channel diameters. Since the desired valve opening time also directly scales with channel diameter, a 10 μm channel would require an opening time of the order of 10–100 ns. Quick-opening valves have successfully be used in millimetre-scale channels (Garen *et al.* 2009), but designing a sufficiently fast valve and integrating it with a microchannel fabricated using surface processes also poses an significant challenge with the available technology. Owing to these difficulties, Giordano, Parisse & Perrier (2008) proposed using a valve to initiate shock tube flow in an intermediate-size (1 mm) channel and then to follow with a contraction into a 100 μm diameter micropipe.

In the present case, we do away with both diaphragm and valve by generating a shock wave in a conventional shock tube and placing the microchannel into this flow, to examine shock wave transmission and propagation into the microchannel.

Since shock waves in gases propagate at speeds of the order of a thousand metres per second and are a few mean free paths in thickness, pressure sensors for the microscale device need to be carefully engineered to achieve proper time and amplitude resolution. To effectively observe the shock propagation in a microchannel, we estimate the required pressure and time resolutions to be of the order 10 kPa and 10 ns, respectively.

There are many known MEMS (microelectromechanical systems) approaches for pressure sensing, the most common using a deformable mechanical element, such as a beam or membrane, whose deflection is translated into a detectable electrical signal by various means. Mechanically, the displacement of a membrane is almost proportional to its smallest lateral dimension. For example, for a 500 nm thick 10 μm square silicon nitride membrane under a 100 kPa pressure difference, the deflection is estimated to be of the order of 50 nm and its natural frequency around 10 MHz, which do not meet the aforementioned required amplitude and time resolutions.

To get away from resolution issues and fabrication complexity associated with membrane-type pressure sensors, we elected to use direct-sensing piezoelectric sensors (Mirshekari & Brouillette 2012). In particular, the piezoelectric sensors fabricated for the present microscale shock tube use very thin films of lead zirconate titanate ceramic (PZT) sandwiched between platinum electrodes. Propagation of shock waves over the sensor surface compresses the PZT film which generates an electrical signal detected via the electrodes. To obtain adequate signal amplitude with acceptable noise from the $M \sim 2$ shock waves of the present experiments, the sensors, and therefore the channels, are designed with large lateral dimensions.

2.2. *Experimental details*

Figure 1 shows the details of the experimental set-up. It comprises a 37.5 mm diameter shock tube, used to generate shock waves at Mach numbers ranging from $M_s = 1.65$ to $M_s = 2.61$, and an instrumented microchannel located near the end of the driven section of the large shock tube. Helium is used as the driver gas and atmospheric air is used as the test gas. Two commercially available fast-response piezoelectric pressure transducers (PCB Piezotronics, model 113A22), mounted on the

https://doi.org/10.1017/jfm.2013.138 Published online by Cambridge University Press

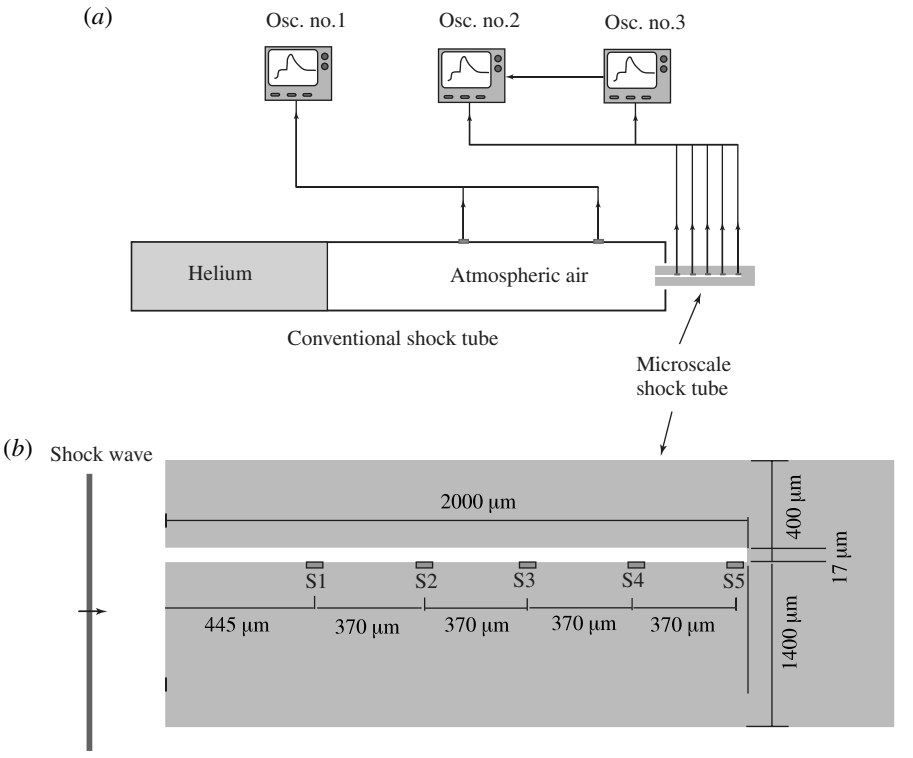


FIGURE 1. Schematic of the experimental set-up (top) and detailed geometry of microscale shock tube (bottom). The driven section of the conventional shock tube has in internal diameter of 37.5 mm. The microchannel has a length of 2000 μm, with a rectangular cross-section of 17 by 2000 μm, for a hydraulic diameter of 34 μm. Each microsensor, identified as S1 to S5, has a breadth of 50 μm along the flow direction and spans the full width of the channel.

driven section of the large shock tube, are used to capture the speed and the pressure jump of the shock wave before it enters the microchannel.

The geometry of the instrumented microchannel is detailed in figure 1. The channel is 2000 μm long, 2000 μm wide and 17 μm high, resulting in a hydraulic diameter of 34 μm in an almost two-dimensional cross-sectional geometry. The channel is equipped with five pressure microsensors at various axial locations along the channel, whose signals are acquired via two synchronized digital storage oscilloscopes. Each of the pressure sensors span the entire 2000 μm width of the channel and extend 50 μm in the direction of shock propagation. The overall thickness of the chip assembly is 1817 μm which is much larger than the height of microchannel and comparable to its length. This ensures that waves originating from the upstream outside corners of the assembly arrive at the microchannel entrance sufficiently late to negligibly affect flow development within the channel during the temporal observation window of interest.

Many of the geometrical specifications of the instrumented microchannel are imposed by the microfabrication techniques used to manufacture the chip (Mirshekari & Brouillette 2012). The first fabrication steps entail a series of etching, deposition and patterning processes of different structural layers on a silicon substrate to fabricate the sensors. This is followed by polymer (SU-8) deposition steps to create the

https://doi.org/10.1017/jfm.2013.138 Published online by Cambridge University Press

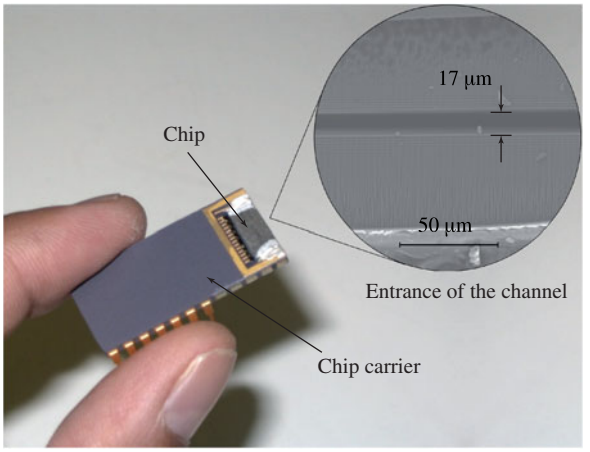


FIGURE 2. (Colour online) Packaging of the chip containing the instrumented microchannel. The inset shows an electron micrograph of the microchannel entrance in a head-on view.

microchannel. A second silicon wafer is bonded to the sensor/channel assembly to close the channel. The entire assembly is then diced to the desired external dimensions and the channel entrance is created by cleaving away part of the assembly. The device is then packaged onto a chip carrier and electrical connections made with the sensor leads.

The pressure microsensors were independently calibrated by operating the microchannel assembly without its silicon cover, thus exposing the microsensors to the same waves as the commercial large-scale transducers mounted at the same axial location along the large shock tube. Since microsensor calibration has been shown to be repeatable from one manufacturing batch to the next, the same calibration was used for the sensors used within the microchannel. With the present data acquisition setup, microsensor sensitivity is $\sim$8.2 mV MPa^{-1} with a minimum detectable pressure of 50 kPa, a frequency response exceeding 1 GHz and an average sensor nonlinearity of 17 %. Because each microsensor has a width of 50 μm in the flow direction, it takes of the order of $\sim$100 ns for a shock wave to travel over each sensor. This means that even an infinitely thin shock wave would exhibit a roughly 100 ns rise time in pressure–time histories.

Figure 2 shows a photograph of the microchannel chip assembly mounted on a chip carrier. An electron micrograph also displays a close-up of the entrance of the microchannel, showing that the microchannel entrance is very uniform. Further details regarding fabrication of the microchannel/sensor assembly are available from Mirshekari (2008) and Mirshekari & Brouillette (2012).

3. Basic flow features

The expected features of the flow being produced within the microchannel first have to be understood to properly interpret the experimental results.

3.1. *Flow around the chip*

The first step is to identify how the flow is being established around the chip, as this determines the entrance boundary conditions for the flow developing within the microchannel. Qualitatively, the interaction of the shock wave generated in the

https://doi.org/10.1017/jfm.2013.138 Published online by Cambridge University Press

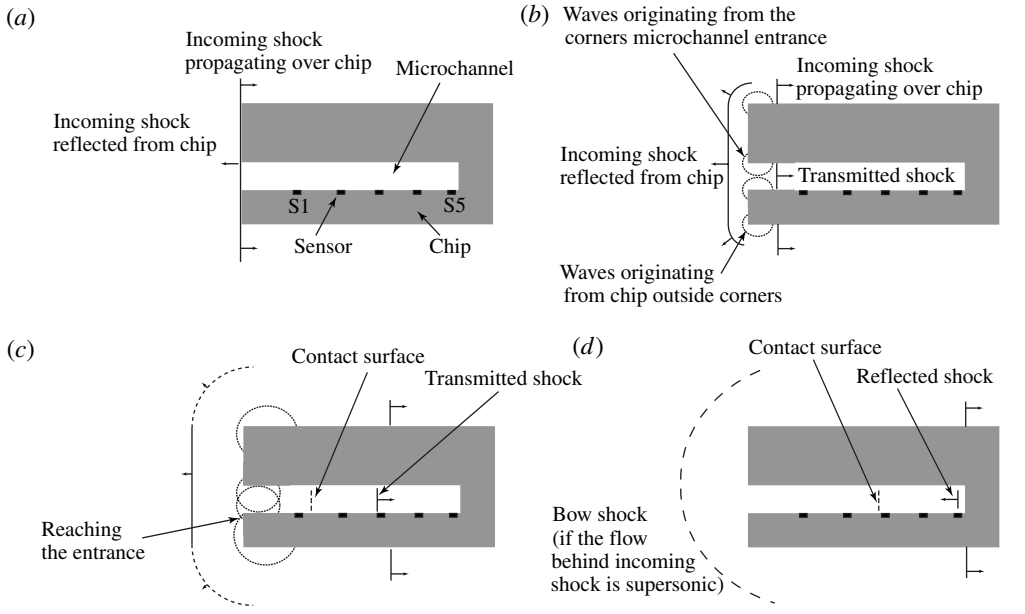


FIGURE 3. Time evolution of the three-dimensional wave patterns following the interaction of the large-scale incoming shock with the chip containing the microchannel. (*a*) Head-on interaction of the shock with the chip. (*b*) Reflected shock propagating upstream, shocks propagating downstream around the chip and within the microchannel, waves propagating away from the outside corners of the chip and from the edges of the microchannel entrance. (*c*) Waves originating from the corners of the chip eventually reach the entrance of the microchannel. A contact surface appears between the gas that was originally within the microchannel and the gas that was initially outside. (*d*) Reflected waves having propagated and decayed away, leaving the chip subject to the steady flow behind the original incoming shock, with a bow shock present if this flow is supersonic.

large-scale shock tube with the chip containing the instrumented microchannel is schematically represented in figure 3. As the incoming shock wave collides head-on with the chip, a reflection takes place from the solid boundary while the shock simultaneously propagates around the chip and within the microchannel (figure 3*a*). At the same time, waves originate from the top and bottom front corners of the chip as well as from the entrance corners of the microchannel (figure 3*b*). The latter waves immediately modify the inlet conditions and thus influence subsequent shock propagation within the microchannel. At a later time, the waves originating from the outside corners of the chip reach the entrance of the microchannel, further modifying the inlet boundary conditions and eventually propagating into the microchannel (figure 3*c*). After a sufficiently long time, the incoming shock has propagated around the chip and the waves reflected from the chip have decayed away, leaving the chip subject to the steady flow established behind the original incoming shock (figure 3*d*); if this flow is supersonic, a bow shock will stand-off a certain distance from the chip.

3.2. *Generic wave diagram*

These processes can best be understood by examining the simplified inviscid one-dimensional wave diagram for the flow along the centreline of the microchannel, as

https://doi.org/10.1017/jfm.2013.138 Published online by Cambridge University Press

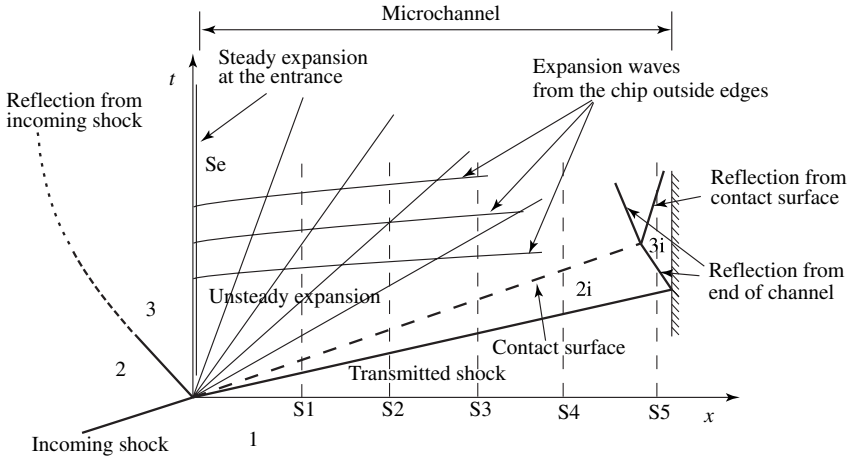


FIGURE 4. Simplified inviscid one-dimensional wave diagram for the flow outside and within the microscale shock tube.

shown in figure 4. State 1 represents the atmospheric quiescent condition initially present in both the large-scale and microscale test sections. The gas in the large shock tube first gets compressed by the incoming shock wave to state 2. The interaction of this shock with the front of the chip produces a reflected shock wave propagating back upstream into the large-scale shock tube and a transmitted shock wave propagating downstream into the microchannel. State 3 is the essentially stagnated gas outside of the entrance, behind the reflected shock. This gas is then accelerated through a steady expansion (se), associated with the area reduction into the microchannel entrance. In the meantime, the transmitted shock wave travels within the microchannel, bringing the fluid to state 2i. In the absence of viscosity, the steady expansion at the channel entrance is caused by a purely converging geometry and the flow may thus be accelerated to a local maximal Mach number of unity. If further expansion is required to match state 2i, then a left-facing centred unsteady expansion is required; because these waves are travelling upstream into a supersonic flow with respect to the fluid, this expansion is actually being swept downstream inside the microchannel. A contact surface also separates the gas processed by the incident shock inside the microchannel from the expanded gas originating from outside of the channel.

This wave diagram supposes that the inlet of the microchannel gets started instantaneously, therefore it assumes that flow changes due to lateral waves originating at the entrance take place at time scale much shorter than those shown in the diagram. Eventually, when the transmitted shock wave reaches the end of the microchannel, a reflected shock wave is produced, bringing the gas to rest at state 3i. Also shown are waves originating from the outside corners of the chip (see figure 3*c*), which reach the microchannel entrance after a certain delay; these subsequently propagate downstream into the microchannel faster than the transmitted shock but never overtake it before it reaches the end wall.

From this wave diagram, qualitative pressure–time histories can be constructed at each sensor station. It is seen that sensors near the channel entrance will first experience a pressure jump due to transmitted shock wave arrival, followed by a gradual pressure increase caused by the unsteady expansion generated at the channel entrance (if present). At later times, the arrival of waves originating from

https://doi.org/10.1017/jfm.2013.138 Published online by Cambridge University Press

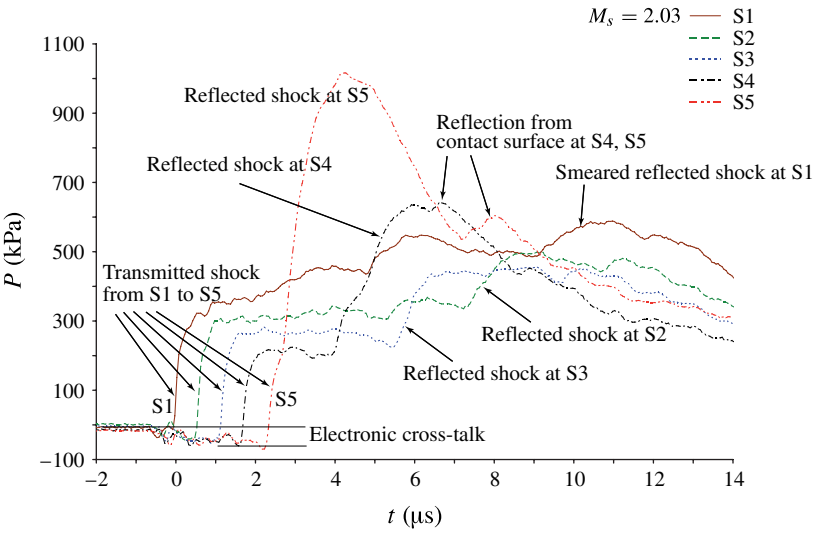


FIGURE 5. (Colour online) Pressure–time histories for the $M_s = 2.03$ experiment, measured at the sensor locations S1 to S5.

the outside corners of the chip will cause another gradual pressure increase. Finally the propagation of the reflected shock from the end of the microchannel will produce another pressure jump. Sensor response near the end of the microchannel is expected to be similar, but dominated by the reflected shock and by its interaction with the contact surface.

4. Experimental results

Shock waves of varying incoming Mach number M_s are produced in the large-scale shock tube. The subsequent transmission and propagation of this wave into the micrometre-scale channel is examined via pressure measurements at the five microsensor locations. Various flow features are then extracted from the measured pressure–time histories and compared over a range of incoming Mach numbers.

4.1. *Flow features*

Figure 5 presents the temporal pressure records at the five stations (S1 to S5) along the microchannel for an experiment performed at $M_s = 2.03$. The general features of these pressure traces are qualitatively similar to those normally observed for shock wave propagation at large scales, but with salient differences.

At each microsensor location, the evolution of pressure starts by a rapid rise in pressure that corresponds to the arrival of the transmitted shock. These features are clearly noticeable from the pressure traces at each microsensor location and are indicated in figure 5. A small negative pressure is initially observed in the experimental pressure histories as the transmitted shock wave propagates from S1 to S5. This is the induced signal caused by electronic crosstalk between the five sensors through the ground connection of the chip (Mirshekari & Brouillette 2012). This negative voltage is subsequently corrected for in quantifying transmitted shock pressure jumps.

https://doi.org/10.1017/jfm.2013.138 Published online by Cambridge University Press

A careful examination of the pressure traces shows that the pressure jump decreases and that the time interval for wave arrival at successive microsensor locations increases as the transmitted shock propagates downstream into the microchannel: this is indicative of shock wave attenuation. The observed rise time for the transmitted pressure jump is of the order of a few hundreds of nanoseconds, and this is not an artefact of the instrumentation since the electronic rise time of each sensor is of the order of a nanosecond. The observed rise time appears constant from S1 to S5, so no observable shock thickening appears to be taking place as the transmitted shock propagates into the microchannel.

Following the pressure jump associated with the arrival of the transmitted shock at sensor station S1, a slower rise in pressure is eventually observed, which indicative of either the action of unsteady expansion waves originating at the entrance of the channel or a pressure drop associated with viscous losses. Accordingly, this gradual pressure rise is less apparent further into the channel, as observed from the pressure traces.

The interaction of the transmitted shock with the end wall of the microchannel produces a reflected shock travelling back upstream, as in large-scale shock tubes. The arrival of this reflected shock at the various sensor locations is indicated in figure 5 for the $M_s = 2.03$ experiment. The features of the reflected wave are complicated, since they are strongly influenced by interactions with: (*a*) the boundary layer developing behind the transmitted wave; (*b*) the contact surface; and (*c*) unsteady expansions originating at the channel entrance. In particular, since the fluid upstream of the contact surface has a higher acoustic impedance than the fluid downstream of it, the interaction of the reflected shock wave with the contact surface is expected to produce two shock waves, one propagating upstream into the channel as well as one reflected back towards the end wall (see figure 4). The eventual arrival of the latter wave at microsensors S4 and S5 has been identified and is indicated in figure 5.

After crossing the contact surface, the amplitude of the pressure rise associated with the upstream-moving reflected shock wave decreases and its duration increases, indicating both attenuation and thickening as a result of interaction with the boundary layer and expansions; this shock wave is clearly observed at sensors S1 to S3, as indicated in the figure. These interactions appear to produce the most attenuation at the midpoint of the channel (near sensor station S3), where the maximum observed pressure is the lowest of all five sensor stations.

4.2. *Influence of Mach number*

Figure 6 shows the pressure records for six other experimental conditions, at incoming shock Mach numbers ranging from $M_s = 1.65$ to $M_s = 2.61$. For all Mach numbers, the pressure–time histories are qualitatively similar to the $M_s = 2.03$ case presented in figure 5.

For all cases, the shock wave transmitted into the microchannel is strongly attenuated in pressure amplitude as well as in velocity. Figure 7 shows the transmitted shock pressure jump, measured at each sensor station, as well as the average transmitted shock velocity, computed from the time of arrival between two successive sensor stations, as a function of normalized axial location. The relative attenuation of the pressure jump is greater for the stronger shocks but the relative attenuation in wave speed is similar for all cases. Also evident is the fact that, for all locations, the Mach number of the transmitted wave is always weaker than that of the incoming wave.

These pressure traces show that the slow pressure rise observed just after the arrival of the transmitted shock at S1 for the $M_s = 2.03$ experiment is absent for

https://doi.org/10.1017/jfm.2013.138 Published online by Cambridge University Press

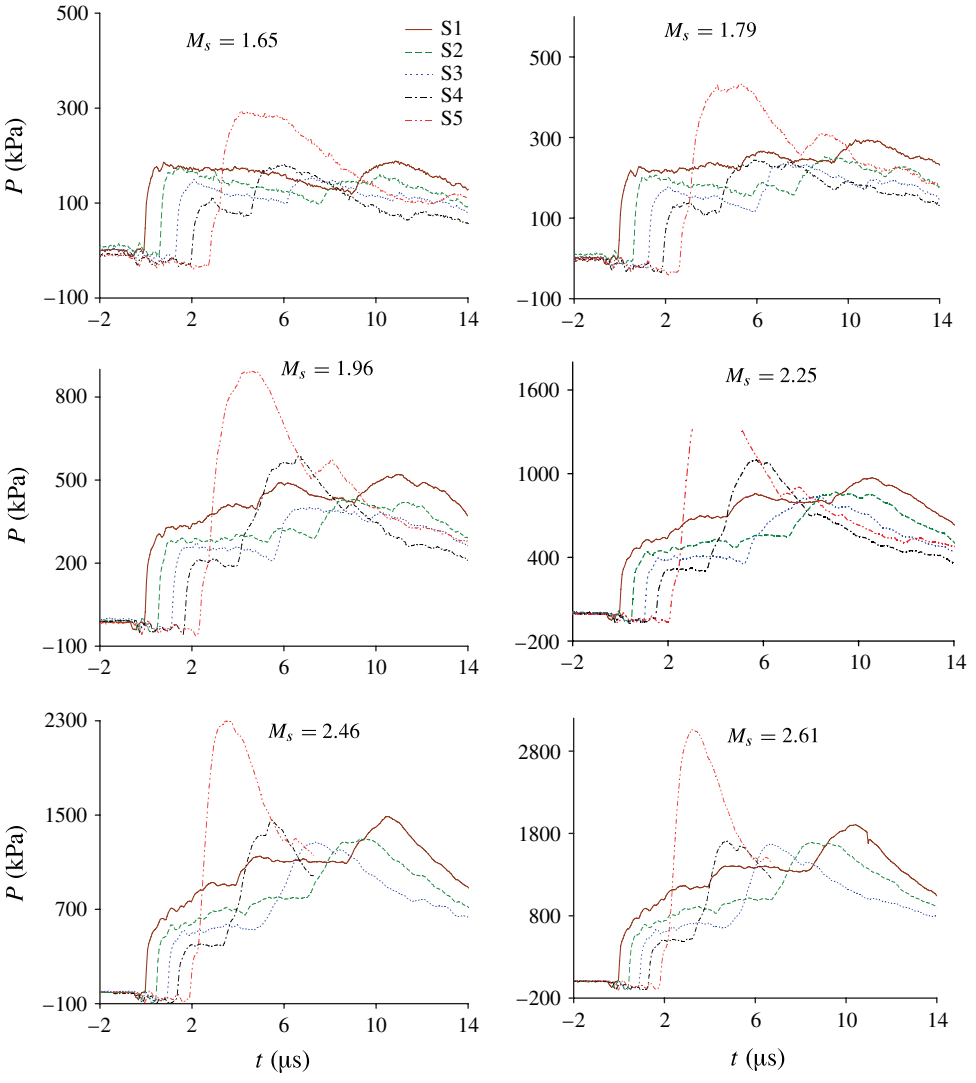


FIGURE 6. (Colour online) Experimental microchannel pressure records for experiments performed at various Mach numbers.

the $M_s = 1.65$ and $M_s = 1.79$ cases, probably due to the absence of the unsteady expansion originating from the microchannel entrance. This gradual pressure rise becomes noticeable at $M_s = 1.96$ and its magnitude increases with incoming Mach number. Furthermore, this pressure rise is only observed at sensor S1 for the $M_s = 1.96$ and $M_s = 2.03$ cases, but can also be seen at more sensor stations as the Mach number is increased; this is consistent with the theoretical appearance of these unsteady expansions only for $M_s > 1.717$ (see § 5.1).

Figure 8 shows wave diagrams for the observed trajectories of both the transmitted and reflected shock waves for all studied cases. Because pressure jumps associated with these waves have a finite duration, the time of arrival of each wave corresponds to the beginning of the pressure rise for each wave. The temporal origin $t = 0$ of these

https://doi.org/10.1017/jfm.2013.138 Published online by Cambridge University Press

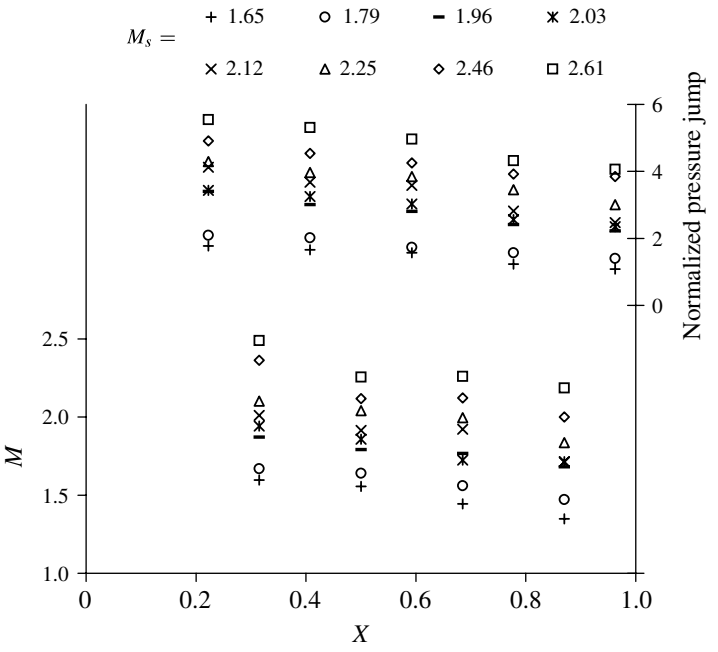


FIGURE 7. Normalized pressure jump and Mach number M of transmitted shock wave propagating into the microchannel shown as a function of normalized axial position. The normalized pressure jump $((p_{after} - p_{before})/p_{before})$ is computed and indicated at each sensor location; the shock wave Mach number is computed from time of arrival measurements between two successive sensors and is thus indicated at the midpoint of the corresponding spatial interval. The axial position is normalized with the microchannel length (2000 μm), with $X = 0$ at the microchannel entrance and $X = 1$ at the end wall.

diagrams was arbitrarily chosen to correspond with the arrival of the transmitted shock wave at the first sensor S1. Logically the fastest and strongest transmitted shock waves are associated with the larger Mach numbers M_s. In the laboratory reference frame, however, the speed of the reflected shock is observed to be similar for all experiments.

Finally, table 1 lists the maximum pressure observed for each experiment, namely the reflected shock pressure at sensor station S5. A 10-fold increase in maximal pressure is observed from $M_s = 1.65$ to $M_s = 2.61$.

5. Flow models

Various flow models have been used to explain the observed results; they range from a simple one-dimensional inviscid analytical model to Navier–Stokes computational fluid dynamics (CFD) computations.

5.1. *Quasi-one-dimensional inviscid adiabatic unsteady model*

Owing to the complex three-dimensional nature of the flow around the chip and within the microchannel, as well as the potential effects of friction and heat transfer, some simplifying assumptions are required in order to render this problem amenable to simple analytic solutions. Here we consider the chip as infinitely thick compared with the microchannel height, thus ignoring waves originating from the chip outside corners; as well, disregarding waves generated at the microchannel entrance assumes

https://doi.org/10.1017/jfm.2013.138 Published online by Cambridge University Press

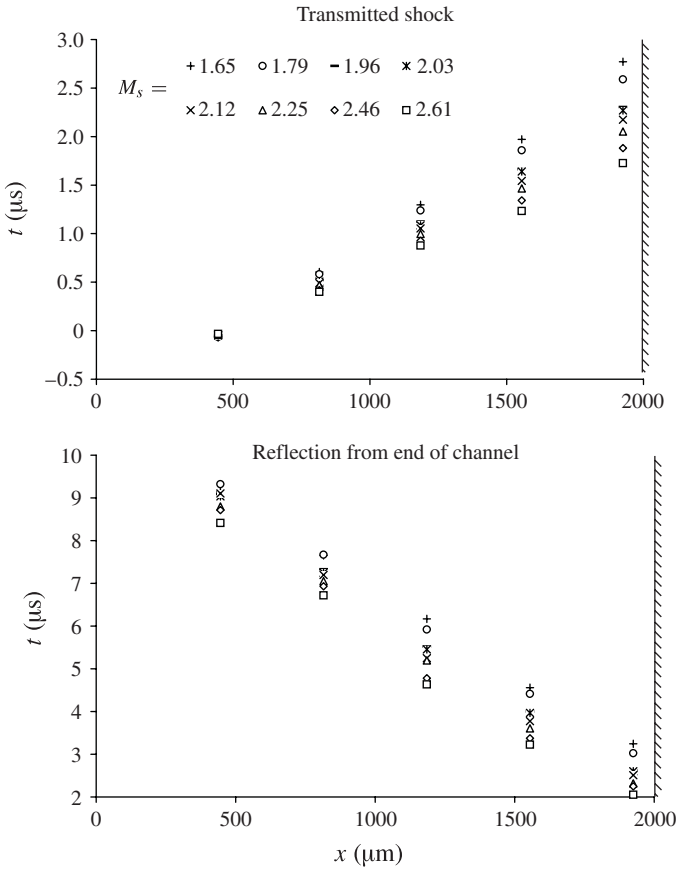


FIGURE 8. Experimental wave diagrams for experiments performed at $M_s = 1.65$ to $M_s = 2.61$. The temporal origin $t = 0$ was chosen to correspond with the arrival of the transmitted shock wave at the first sensor S1.

Incoming Mach number M_s	Maximum reflected shock pressure (kPa)	
	Experimental (at S5)	Quasi one-dimensional model
1.65	320	1324
1.79	460	1766
1.96	930	2412
2.03	1060	2712
2.12	1280	3111
2.46	2320	4913
2.61	3180	5853

TABLE 1. Maximum pressure behind microchannel reflected shock for various incoming Mach numbers.

that the inlet gets started instantaneously. As a consequence, the problem becomes a simple one of interaction of a shock wave with an infinitely small orifice; we further

https://doi.org/10.1017/jfm.2013.138 Published online by Cambridge University Press

neglect friction and heat transfer and consider the fluid as an ideal gas, as with the analysis of Laporte (1955).

Based on the flow model of § 3.1, the gas outside the microchannel entrance is processed by the incoming shock and by its reflection from the chip. Owing to the large area ratio between the shock tube and the microchannel, the conditions behind the reflected shock can be assumed to correspond to those at an impermeable wall, with the gas being brought to rest by the reflected shock before entering the microchannel. This gas then expands isentropically into the microchannel through the area contraction and this high-speed flow then drives a shock wave downstream into the microchannel (figure 4). This inviscid adiabatic analytical model utilizes the usual ideal gas one-dimensional unsteady flow models for shock and expansion wave propagation as well as a quasi-one-dimensional steady isentropic solution at the microchannel entrance. The resulting flow is simply obtained by matching the flow properties of the different flow regions in pressure–velocity space.

Figure 9 shows pressure–velocity (p–u) diagrams for the flow processes described above for $M_s = 1.65$ and $M_s = 2.61$. In these graphs, the initial state in both the large-scale shock tube and the microchannel is quiescent air at atmospheric pressure, shown as state 1 in the figure. The loci of all possible conditions behind a shock wave propagating to the right into this gas at rest are shown on the solid curve emerging from state 1; in the present case the incoming shock brings the gas to state 2. From this state, the loci of all possible conditions behind a reflected shock wave propagating to the left are shown on the solid curve emerging from state 2. Because state 3 has been assumed at rest, the solution for this state is found on the reflected shock curve at $u = 0$. This stagnated air at elevated pressure then expands steadily and isentropically into the microchannel via an area reduction, which increases flow velocity and reduces pressure, a process indicated on the figure by the dashed curve emerging from state 3. Because of the purely converging geometry, maximal expansion by this process may eventually choke the flow, to conditions indicated by a circle on the dashed curve. While these processes are taking place outside, a shock is transmitted into the microchannel, processing the flow from state 1, along the same shock wave curve as the incoming shock, to an unknown state 2i to be determined.

The gas originally at rest within the microchannel and processed by this transmitted shock wave is separated from the gas originating outside the channel by a contact surface across which both velocity and pressure must be continuous. As a consequence, the solution for state 2i is obtained by the intersection in p–u space of the steady isentropic expansion from state 3 with the shock wave from state 1, as shown in figure 9(a) for $M_s = 1.65$. In this case, the steady isentropic expansion intersects the shock curve before choking the flow, leading to a subsonic end state 2i behind the contact surface. One should note that temperatures and densities maybe different across the contact surface, since the state behind the contact surface has been processed by the incoming shock, the reflected shock and the expansion while the state ahead of the contact surface has only been processed by the transmitted shock.

When the steady isentropic expansion process, terminated by the choked flow condition in a purely converging geometry, cannot reach the 1–2i shock curve, the flow is further accelerated by a left-facing centred unsteady expansion, indicated on figure 9(b) ($M_s = 2.61$) by a dotted line. The intersection of this expansion with the shock curve leads, in this case, to a supersonic end state 2i behind the contact surface. According to this model, this unsteady expansion will appear at the microchannel entrance for an incoming Mach number $M_s > 1.717$ in air at atmospheric initial conditions.

https://doi.org/10.1017/jfm.2013.138 Published online by Cambridge University Press

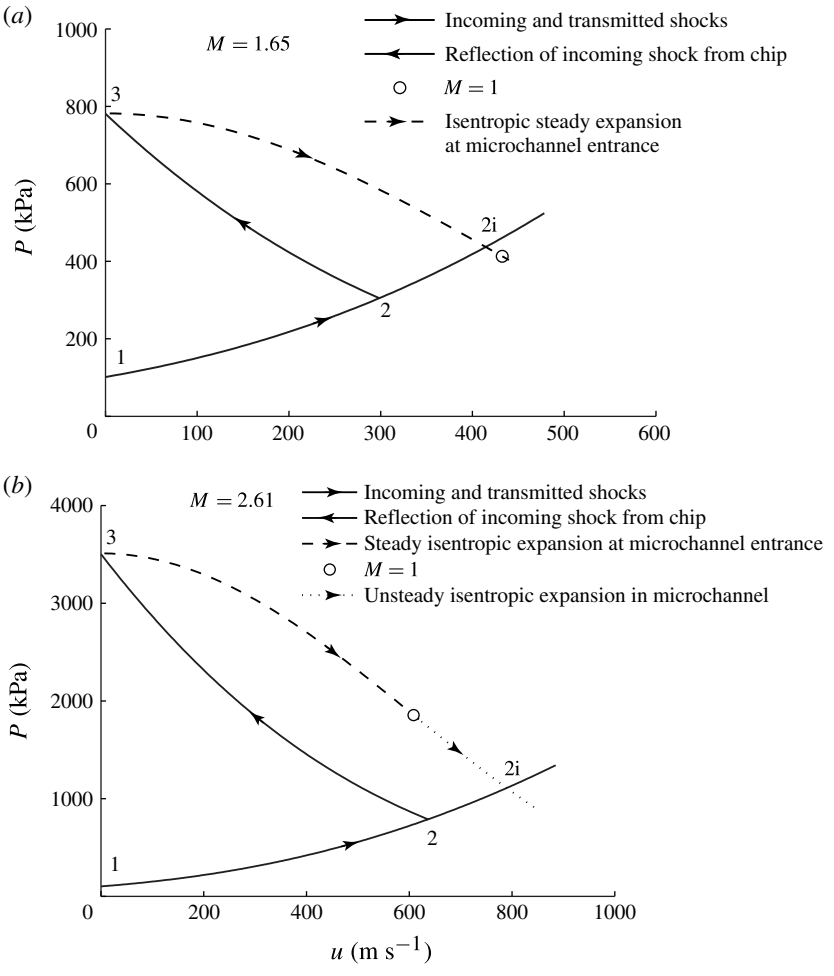


FIGURE 9. Pressure–velocity diagrams for the one-dimensional inviscid adiabatic unsteady model: (*a*) $M_s = 1.65$; for this condition the steady subsonic isentropic expansion through the convergent inlet is sufficient to expand the flow to state 2i behind the transmitted shock; therefore the inlet of the microchannel is not choked in this case; (*b*) $M_s = 2.61$; for this condition the steady subsonic isentropic expansion through the convergent inlet is not sufficient to expand the flow to state 2i behind the transmitted shock; therefore the inlet of the microchannel is choked in this case and the additional required flow acceleration is provided by a left-facing centred unsteady expansion.

This model predicts that the shock transmitted into the microchannel is always stronger than the incoming shock for all Mach numbers (figure 10), the result of the converging geometry. Also, in the absence of flow losses and for an infinitely thick chip, the transmitted wave maintains a constant strength along the microchannel: no shock attenuation is therefore possible with this model, as shown in figure 11.

Within the same model assumptions, the reflection of the transmitted shock at the end of the microchannel can also be computed assuming that the gas is brought to rest at the end wall. The resulting reflected shock pressures are shown in table 1, with values greatly above those observed in the experiments.

https://doi.org/10.1017/jfm.2013.138 Published online by Cambridge University Press

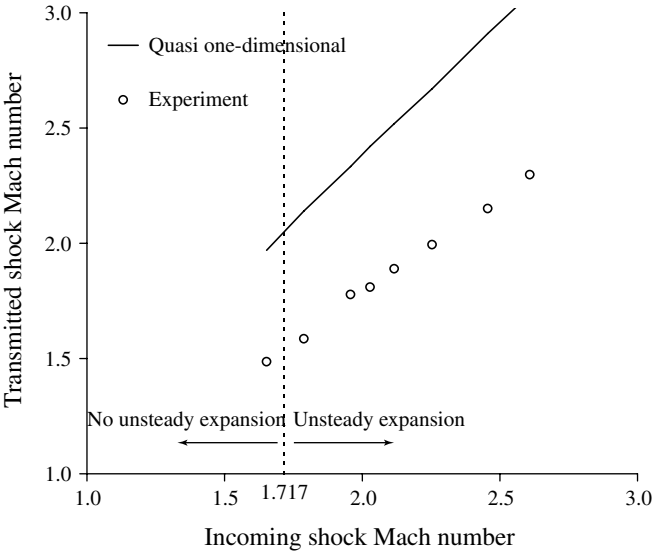


FIGURE 10. Transmitted shock Mach number M in the microchannel versus incoming shock Mach number, computed from quasi-one-dimensional inviscid adiabatic model.

5.2. *Euler numerical computations*

The flow is also modelled numerically using a two-dimensional Euler code with adaptive mesh refinement (Quirk 1998) which has been extensively validated against appropriate experiments. Although of limited usefulness to capture the flow developing within the microchannel because of the inviscid flow hypothesis, the Euler computation is nevertheless computationally effective to capture the flow around the chip in order to determine the time evolution of the microchannel entrance conditions.

Towards that end, two-dimensional computations were performed for the geometry shown in figure 1 for both the flows outside and inside the microchannel. The computation domain was assumed to be symmetric about the microchannel centreline and, as a worse case, the overall chip thickness was taken to be 800 μm instead of 1800 μm. The computational domain is mapped with a structured grid of 8.5 μm cell^{-1} base resolution in both directions, with the cell dimensions iteratively halved up to five times as the need arises, leading to a maximum resolution of $8.5/2^5 = 0.26$ μm cell^{-1} in regions of strong density and/or pressure gradients. The time steps are dynamically determined at the beginning of each iteration so that a CFL condition (Courant, Friedrichs & Lewy 1928) of 0.8 is respected.

These simulations allow for the computation of the flow properties within the microchannel, subject to the model assumptions. For example, the transmitted shock Mach number is shown as a function of axial position in figure 11 for the $M_s = 2.61$ case. It is seen that there is an important flow starting region near the microchannel entrance, in which the shock accelerates rapidly, followed by more gradual acceleration towards the shock speed computed from the quasi-one-dimensional inviscid adiabatic model. Even with a microchannel length-to-height ratio of nearly 60, the Euler solution has not yet reached asymptotic conditions, underscoring the strong influence of inlet start-up in this simulation.

https://doi.org/10.1017/jfm.2013.138 Published online by Cambridge University Press

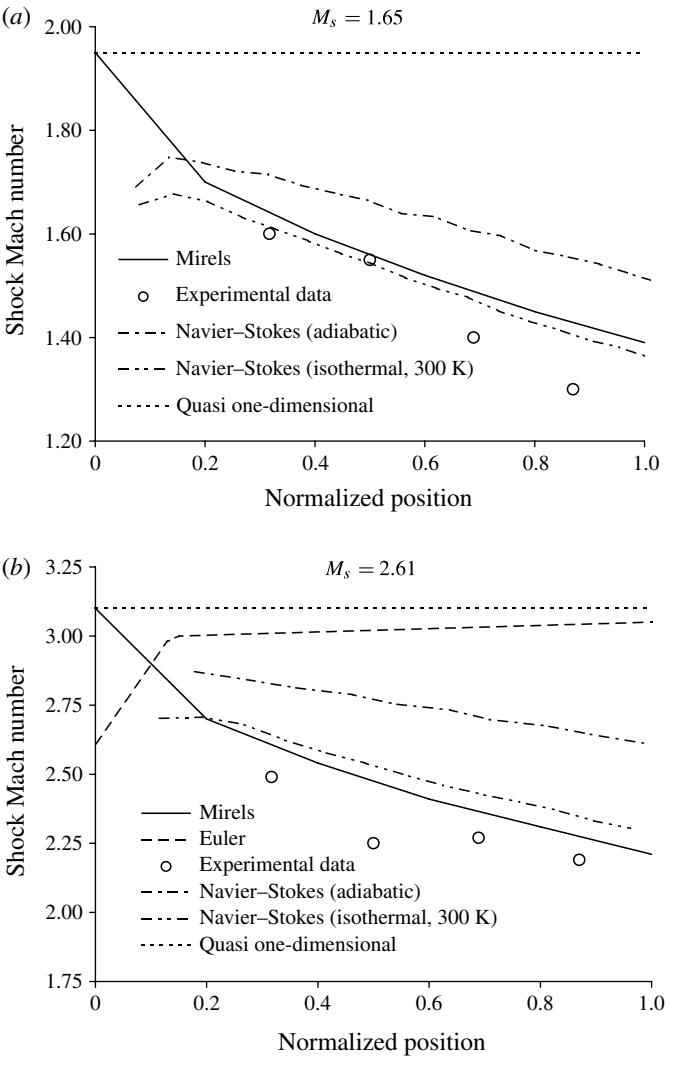


FIGURE 11. Transmitted shock Mach number M as a function of position: comparison between experiments and models. Incoming shock: (*a*) $M_s = 1.65$ and (*b*) $M_s = 2.61$.

Within the model assumptions, the Euler simulations are better suited for the computation of the flow around the chip; of particular interest is the pressure near the inlet of the microchannel. Figure 12 shows pressure distributions upstream of the microchannel entrance along the microchannel centreline as a function of time, for both $M_s = 1.65$ and $M_s = 2.61$ cases. The results show that the stagnated gas pressure in the inlet region initially corresponds closely to the reflected shock pressure computed from the quasi-one-dimensional inviscid adiabatic model. We also note that, after a certain time, this pressure decreases, due to the arrival of expansion waves originating from the chip front external corners, as described in figure 3(*c*). The Euler computations are useful to determine the period over which the maximum inlet pressure is constant, and this ranges from 0.82 μs for the $M_s = 1.65$ case to 0.59 μs for $M_s = 2.61$. The weak waves from the corners of the chip eventually enter the

https://doi.org/10.1017/jfm.2013.138 Published online by Cambridge University Press

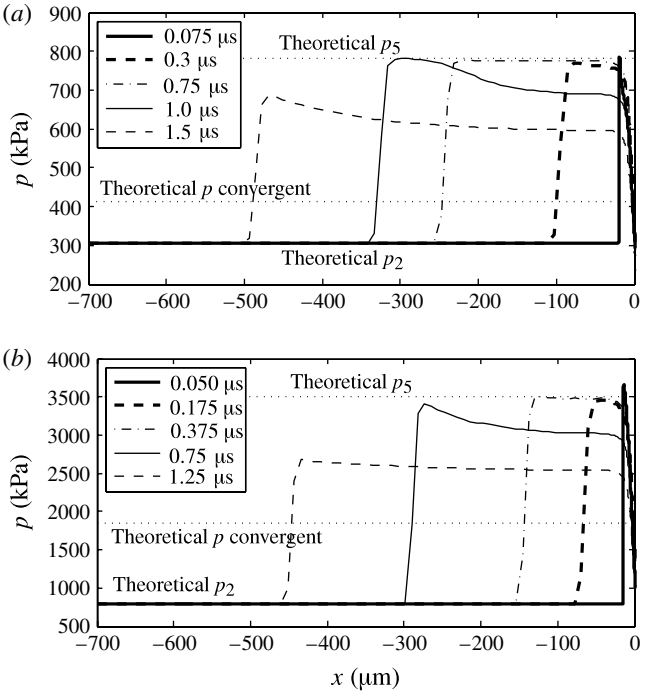


FIGURE 12. Pressure distributions upstream of the microchannel inlet along microchannel centreline, obtained from Euler numerical computation. Inlet at $x = 0$ μm. Time origin is when incoming shock wave arrives at inlet. Incoming shock: (*a*) $M_s = 1.65$ and (*b*) $M_s = 2.61$. Theoretical p_2 is the theoretical pressure behind the incoming shock and theoretical p_5 is the computed reflected shock pressure from an impermeable wall, both computed from one-dimensional perfect gas normal shock relations. Theoretical p convergent is the computed pressure at the inlet of the microchannel, assuming an isentropic steady expansion of a perfect gas from p_5.

microchannel and travel at a speed equal to the local speed of sound added to the local flow velocity. The speed of these waves is actually greater than the transmitted shock speed, but they never catch up with the shock. Their propagation into the microchannel can nevertheless be clearly detected from the experimental pressure–time histories, as seen for example in figure 5.

5.3. *Navier–Stokes numerical computations*

The flow is also modelled numerically using the two-dimensional finite-volume Navier–Stokes code CARBUR, which offers second-order resolution for both spatial and time derivatives and uses a Van-Leer flux limiter with a MUSCL scheme; more details about CARBUR can be found in Burtschell, Cardoso & Zeitoun (2001). The simulation uses a no-slip kinematic wall condition and either isothermal (300 K) or adiabatic walls. No-slip kinematic and thermal wall boundary conditions can be applied with confidence in this computation since the maximal Knudsen number is ∼0.002 in the present experiments (Arkilic, Schmidt & Breuer 1997).

In this case the chip is assumed to be infinitely thick, with appropriate through-flow boundary conditions upstream of the microchannel following incoming shock wave reflection. From symmetry considerations, only the top half of the flow

https://doi.org/10.1017/jfm.2013.138 Published online by Cambridge University Press

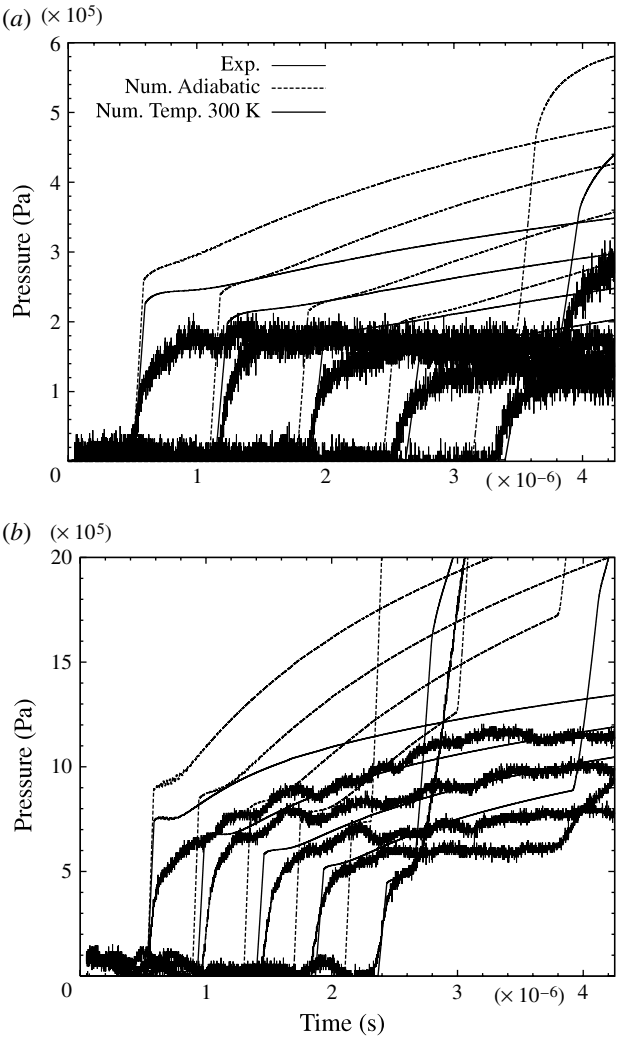


FIGURE 13. Pressure–time histories at the five transducer locations: comparison between experiment (Exp.), Navier–Stokes isothermal wall at 300 K (Num. Temp. 300 K) and adiabatic wall (Num. Adiabatic) computations. Incoming shock: (*a*) $M_s = 1.65$ and (*b*) $M_s = 2.61$.

field is computed, using 39 lateral cells (cell width of 0.22 μm), with a reflecting boundary condition imposed on the channel centreline. The first 200 μm length of the microchannel is meshed with 599 axial cells (cell length of 0.33 μm), and the rest of the channel (1800 μm) is meshed with 9 blocks of 399 cells (cell length of 0.5 μm); a CFL condition of 0.5 is used throughout. Results from the Navier–Stokes computations can directly be compared with the experimental pressure traces by spatially averaging the computed wall pressure signal over each sensor footprint. For example, figure 13 shows a comparison between the experiments and Navier–Stokes isothermal (300 K) and adiabatic computations for the pressure–time histories at the five transducer locations for an incoming shock at $M_s = 1.65$ and $M_s = 2.61$. We observe that the adiabatic computation overpredicts both the amplitude and the speed of the transmitted

https://doi.org/10.1017/jfm.2013.138 Published online by Cambridge University Press

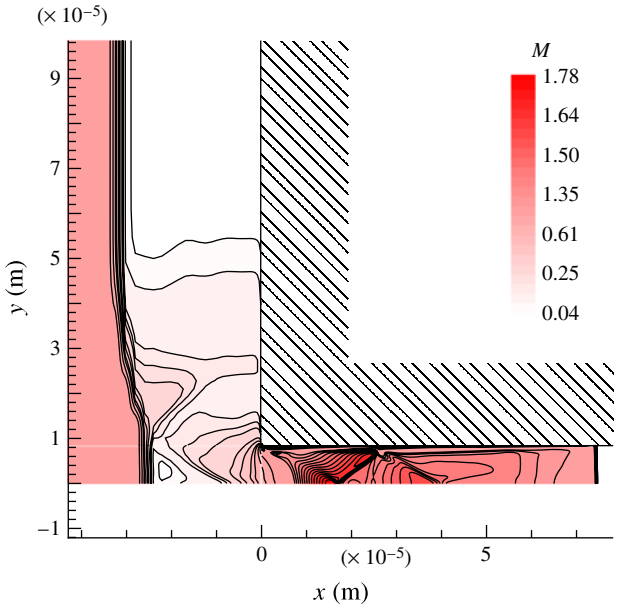


FIGURE 14. (Colour online) Contour plot of Mach number in the microchannel entrance region at $t = 0.2$ μs after arrival of the incoming shock at inlet. Results from Navier–Stokes isothermal wall computation with $M_s = 2.61$.

shock, while the isothermal model captures quite well the shock velocity, the shock pressure jump and the subsequent observed pressure increase behind the shock. Similar comparisons at the other tested Mach number lead to the same conclusions.

Figure 11, showing the evolution of the speed of the transmitted shock wave, also incorporates the Navier–Stokes results. It is clear that the isothermal wall conditions produce a shock speed decay more in line with the experimental results over the range of tested Mach numbers.

The Navier–Stokes computations also allow for the examination of the microchannel entrance region in great detail. Of great importance, these simulations show the presence of a vena contracta at the microchannel entrance due to viscous flow separation at the sharp inlet corners (figure 14). In effect, this creates a converging–diverging geometry at the inlet, which differs from the actual converging geometry of the device. Owing to this, the stagnated flow outside of the microchannel can undergo a quasi-steady supersonic expansion past the sonic point, up to $M \sim 1.7$ as seen from figure 14 for the $M_s = 2.61$ case. This is a significant departure from the quasi one-dimensional inviscid adiabatic model, which only allowed a quasi-steady expansion up to sonic conditions, and this can play a significant role in the determination of the downstream flow, especially the transmitted shock properties.

5.4. *Boundary layer model*

Owing to the development of a boundary layer behind the transmitted shock, negative displacement thickness effects cause the Mach number of the shock $M(x)$ to attenuate (Mirels 1966). Order of magnitude estimates show that the boundary layer Reynolds number, based on the shock propagation distance, is of the order of 10^5, thus the boundary layer behind the transmitted shock can be assumed to be laminar. As well,

https://doi.org/10.1017/jfm.2013.138 Published online by Cambridge University Press

the laminar boundary layer thickness can be shown to never exceed the channel half-width, an indication that the flow can be treated as not fully developed. Within those assumptions, the evolution of the transmitted shock wave Mach number can be expressed as

$$M_s(x) = M_s(0)\left(1 - C\left(\frac{x}{D}\right)^{1/2}(p_1 D)^{-1/2}\right) \tag{5.1}$$

with x the shock travel distance from the microchannel entrance and p_1 the initial pressure in the microchannel (here 1 atm); the constant C is calculated from the laminar boundary layer solution of Mirels (1966), with $C \approx 0.0020$ kPa^{-2} m^{-2} for the present experimental conditions, as reported by Russell (1966). The initial transmitted shock Mach number $M(0)$ is computed from the quasi-one-dimensional inviscid adiabatic unsteady model.

These results are compared with the experiments and the other models in figure 11. It is seen that there is very good agreement between the boundary layer model and the Navier–Stokes isothermal computations, and good agreement with the experimental results, underscoring that the laminar non-developed hypothesis is appropriate for the present situation.

6. Discussion

The flow models of the previous section can be compared with the experimental results to gain insight into the fluid mechanics of shock wave transmission into a microchannel. Figure 11, showing the spatial evolution of the transmitted shock Mach number, shows that the two-dimensional Navier–Stokes isothermal computations and the simple laminar boundary layer model achieve the best agreement with the experimental results. This underscores that, in the present case, the flow remains laminar and is dominated by the development of the boundary layer along the microchannel. Obviously both inviscid models, namely the quasi-one-dimensional unsteady analytical model and the Euler numerical computation, are fundamentally inadequate for this microchannel flow dominated by viscous effects.

Better agreement is achieved with the isothermal Navier–Stokes computation than with the adiabatic computation, and this is indicative of the importance of the thermal boundary layer developing along the microchannel walls. At these scales it is not surprising that convective wall heat transfer is significant (e.g. Guo & Li 2003).

In theory, the quasi-one-dimensional unsteady analytical model could be modified to include viscous and heat transfer effects, for example by including Fanno and/or Rayleigh flow processes between the microchannel inlet and the contact surface and/or the shock. However, the steady flow hypothesis associated with these classical flow solutions is not compatible with the inherent unsteadiness of the present flow.

Heuristically, the present flow can be understood by viewing the inlet mass flux as driving the contact surface, here acting as a massless piston, whose motion is itself responsible for driving the transmitted shock into the microchannel. Because the inlet flow can reasonably assumed to be steady before the arrival of expansions from the chip corners, as shown in figure 12, then the mass flow entering the microchannel is constant over this period. If the microchannel flow were inviscid, then the velocity of the contact surface would be constant to accommodate the steady inlet mass flow rate. This, in turn, would drive a constant velocity shock, corresponding to the inviscid flow solution.

https://doi.org/10.1017/jfm.2013.138 Published online by Cambridge University Press

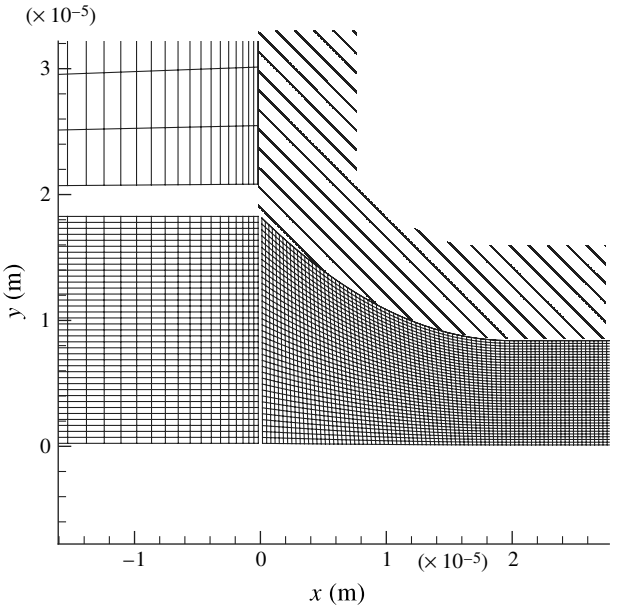


FIGURE 15. Rounded entrance geometry for Navier–Stokes isothermal wall computation: details of the mesh.

However, because of the development of viscous and thermal boundary layers along the microchannel walls, some of the mass entering the microchannel accumulates near the wall, reducing the mass flow available to drive the contact surface, thereby leading to a weaker shock than in the inviscid case. Furthermore, as the boundary layer develops in space and time behind the contact surface, more mass is entering the boundary layer, leading to a decay in contact surface velocity. Assuming laminar boundary layer flow, simple dimensional arguments show that contact surface velocity should decrease as the inverse square root of downstream distance. Similar boundary layer development takes place between the contact surface and the transmitted shock wave, as per the classical Mirels (1966) model. The decay in contact surface velocity, as well as laminar boundary layer development behind the shock, in turn leads to a decay in shock velocity proportional to the square root of distance as seen in § 5.4.

Owing to the observed flow separation due to the sharp corners at the microchannel entrance (figure 14), the inlet flow gets choked at a smaller section than the actual microchannel dimensions. Eliminating this inlet flow separation would lead to greater inlet mass flow rate which, according to the above arguments, would produce a stronger transmitted shock. To test this hypothesis, a Navier–Stokes isothermal wall computation was performed with a rounded channel entrance, as shown in figure 15; the results for the simulated pressure sensor time histories are shown in the geometry of figure 16. As compared with the actual (square) entrance experimental results and computation, the results for the computation with the rounded entrance indeed produces faster and stronger waves, underlining the critical contribution of the inlet mass flux to the transmitted shock wave propagation into the microchannel.

The model of Brouillette (2003) for microscale shock wave propagation suggests that microscale effects should become important for a ReD/L scaling parameter around unity or lower. In the present experiments, the scaling number for the present situation

https://doi.org/10.1017/jfm.2013.138 Published online by Cambridge University Press

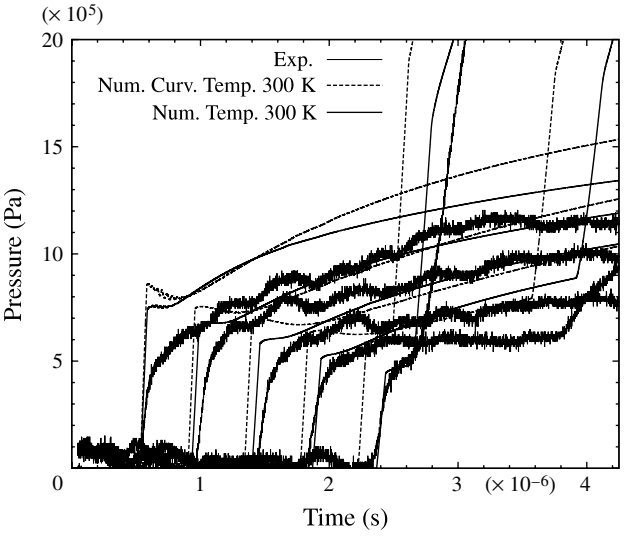


FIGURE 16. Pressure–time histories at the five transducer locations: comparison between experiment (Exp.) and Navier–Stokes isothermal wall computations for actual (Num. Temp. 300 K) and rounded (Num. Curv. Temp. 300 K) channel entrance geometries. Incoming shock $M_s = 2.61$ (bottom).

is relatively large, i.e. $ReD/L \sim O(10 - 100)$, which should not result in important microscale effects for the properties of the transmitted shock wave. Indeed, the observed experimental shock jump conditions are very close to those corresponding to the usual ideal gas model, even though the microchannel hydraulic diameter is only 34 μm; similar conclusions are reached with a one-dimensional numerical model (Mirshekari & Brouillette 2009). Also, in the low scaling parameter limit, the entire flow field is expected to be isothermal, which was not observed in the present Navier–Stokes computations. To observe important microscale shock wave effects in the present experimental configuration, we conclude that the width of the microchannel would have to be reduced by at least an order of magnitude.

7. Conclusions

A microscale fully instrumented shock tube, which is believed to be the smallest ever built to this date, has been fabricated and tested. This facility was used to study the penetration of an incident shock wave, produced in a large (37 mm) shock tube, into the 34 μm hydraulic diameter and 2 mm long microchannel. Pressure microsensors of a novel design, located at five axial stations, were used to obtain pressure–time histories of the shock wave transmitted into the microchannel. In all cases the transmitted shock is found to be weaker than the incident shock and is observed to decay both in pressure and velocity as it travels down the microchannel. These results are compared with various analytical and numerical models, and the best agreement is obtained with a Navier–Stokes CFD computation, which assumes a no-slip isothermal wall boundary condition, as well as with a simple laminar boundary layer model. It is found that the flow developing within the microchannel is also highly dependent on conditions at the microchannel entrance, which determine the mass flux into the microchannel.

https://doi.org/10.1017/jfm.2013.138 Published online by Cambridge University Press

Regardless of the micrometre-size dimensions of the present facility, shock wave propagation in a microchannel of that scale exhibits a behaviour corresponding to the ideal gas shock wave propagation model and the shock attenuation can be explained in terms of accepted laminar boundary layer models. In order to observe more important microscale effects on shock wave propagation, future microchannels should therefore have submicrometre hydraulic diameters or be operated at reduced pressures.

Acknowledgements

This work was supported by the Natural Sciences and Engineering Research Council (NSERC) of Canada. Also, the first author acknowledges the Iranian Ministry of Science, Research and Technology (MSRT) for the scholarship awarded.

REFERENCES

ARKILIC, E. B., SCHMIDT, M. A. & BREUER, K. S. 1997 Gaseous slip flow in long microchannels. *J. Microelectromech. Syst.* **6** (2), 167–178.

AUSTIN, J. & BODONY, D. J. 2011 Wave propagation in gaseous small-scale channel flows. *Shock Waves* **21** (6), 547–557.

BROUILLETTE, M. 1991 Design modifications to T5 and their implementation. *Tech. Rep.* FM 91-3. Graduate Aeronautical Laboratories, California Institute of Technology.

BROUILLETTE, M. 2003 Shock waves at microscales. *Shock Waves* **13** (1), 3–12.

BURTSCHELL, Y., CARDOSO, M. & ZEITOUN, D. E. 2001 Numerical analysis of the reducing driver gas contamination in impulse shock tunnels. *AIAA J.* **12**, 2357–2365.

COLIN, S. 2005 Rarefaction and compressibility effects on steady and transient gas flows in microchannels. *Microfluid Nanofluid* **1** (8), 268–279.

COURANT, R., FRIEDRICHS, K. & LEWY, H. 1928 Über die partiellen differenzengleichungen der mathematischen physik. *Math. Ann.* **100** (1), 32–74.

DOLLING, D. S. 2001 Fifty years of shock-wave/boundary-layer interaction research: What next? *AIAA J.* **39** (8), 1517–1531.

DUFF, R. E. 1959 Shock-tube performance at low initial pressure. *Phys. Fluids* **2** (2), 207–216.

GAREN, W., MEYERER, B., UDAGAWA, S. & MAENO, K. 2009 Shock waves in mini-tubes: influence of the scaling parameter s. In *Proceedings of 26th International Symposium on Shock Waves* (ed. K. Hanneman & F. Seiler), pp. 1473–1478. Springer.

GIORDANO, J., PARISSE, J. D. & PERRIER, P. 2008 Numerical study of an original device to generate compressible flow in microchannels. *Phys. Fluids* **20**, 096101.

GUO, Z.-Y. & LI, Z.-X. 2003 Size effect on microscale single-phase flow and heat transfer. *Intl J. Heat Mass Transfer* **46** (1), 149–159.

IANCU, F. & MULLER, N. 2006 Efficiency of shock wave compression in a microchannel. *Microfluid. Nanofluid.* **2** (3), 50–63.

KIRCHHOFF, C. 1868 Ueber den einçuss der warmeleitung in einem gase auf die schallbewegung. *Pogg. Ann.* **134**, 177–193.

LAPORTE, O. 1955 On the interaction of a shock with a constriction. *Tech. Rep.* LA-1740. Los Alamos Scientific Laboratory.

LEE, J. J., FROST, D. L., LEE, J. H. S. & DREMIN, A. 1995 Propagation of nitromethane detonations in porous media. *Shock Waves* **5**, 115–119.

LEVY, A., SOREKA, S., BEN-DOR, G. & SKEWS, B. 1996 Waves propagation in saturated rigid porous media: analytical model and comparison with experimental results. *Fluid Dyn. Res.* **17**, 49–65.

MAHESH, K., LELE, S. K. & MOIN, P. 1997 The influence of entropy fluctuations on the interaction of turbulence with a shock wave. *J. Fluid Mech.* **334**, 353–379.

MARTEL, E. & BROUILLETTE, M. 2003 Micro-blast waves at subatmospheric pressures. *Comput. Fluid Dyn.* **12** (2), 23–34.

https://doi.org/10.1017/jfm.2013.138 Published online by Cambridge University Press

MIRELS, H. 1957 Attenuation in a shock tube due to unsteady-boundary-layer action. *Tech. Rep.* TN 1333. National Advisory Committee for Aeronautics.

MIRELS, H. 1966 Correlation fomulas for laminar shock tube boundary layer. *Phys. Fluids* **9** (7), 1265–1272.

MIRSHEKARI, G. 2008 Microscale shock tube. PhD thesis, University of Sherbrooke.

MIRSHEKARI, G. & BROUILLETTE, M. 2009 One-dimensional model for microscale shock tube flow. *Shock Waves* **19** (1), 25–38.

MIRSHEKARI, G. & BROUILLETTE, M. 2012 Microscale shock tube. *J. Microelectromech. Syst.* **99**, 1–10.

NGOMO, D., CHAUDHURI, A., CHINNAYYA, A. & HADJADJ, A. 2010 Numerical study of shock propagation and attenuation in narrow tubes including friction and heat losses. *Comput. Fluids* **39**, 1711–1721.

PARISSE, J. D., GIORDANO, J., PERRIER, P., BURTSCHELL, Y. & GRAUR, I. A. 2009 Numerical investigation of micro shock waves generation. *Microfluid. Nanofluid.* **6** (5), 699–709.

QUIRK, J. J. 1998 Amrita—A computational facility (for CFD modelling). In *VKI 29th CFD Lecture Series*, von Kármán Institute for Fluid Dynamics, Brussels, 23–27 February 1998.

ROSHKO, A. 1960 On flow duration in low-pressure shock tubes. *Phys. Fluids* **3** (6), 835–842.

RUSSELL, D. A. 1966 Shock-wave strengthening by area convergence. *J. Fluid Mech.* **27**, 305–314.

SQUIRES, T. M. & QUAKE, S. R. 2005 Microfluidics: Fluid physics at the nanoliter scale. *Rev. Mod. Phys.* **77** (3), 977–1026.

STEWART, D. S. 2002 Towards the miniaturization of explosive technology. *Shock Waves* **11**, 467–473.

TAKAYAMA, K. 1999 Applications of shock wave research to medicine. In *Proceedings of 22nd International Symposium on Shock Waves* (ed. G. J. Ball, R. Hillier & G. T. Roberts), pp. 321–326.

UDAGAWA, S., GAREN, W., MEYERER, B. & MAENO, K. 2008 Motion analysis of a diaphragmless driver section for a narrow channel shock tube. *Shock Waves* **18** (5), 345–351.

ZEITOUN, D. E. & BURTSCHEL, Y. 2006 Navier-stokes computations in micro shock tubes. *Shock Waves* **15** (3–4), 241–246.

https://doi.org/10.1017/jfm.2013.138 Published online by Cambridge University Press